JOURNAL OF THERMOPHYSICS AND HEAT TRANSFER
Vol. 16, No. 4, October–December 2002

Numerical Simulations of Magnetic Flow Control in Hypersonic Chemically Reacting Flows

Henri-Marie Damevin* and Klaus A. Hoffmann†
Wichita State University, Wichita, Kansas 67260-0044

Hypersonic flows over blunt bodies subject to magnetic fields are numerically investigated. The magnetogasdynamic equations in the high magnetic Reynolds number formulation form an eight-equation system, with density, momentum, magnetic field, and total energy as unknowns. In the low magnetic Reynolds number approximation, the magnetic field induction is ignored, which leads to a five-equation system, where the magnetic interaction is represented by source terms in the momentum and energy equations. A four-stage modified Runge–Kutta scheme with the Davis–Yee symmetric total variation diminishing model as a postprocessing stage is used to solve the magnetogasdynamic equations. High-temperature effects are simulated by equilibrium and nonequilibrium chemistry models. The equilibrium model computes thermodynamic properties by interpolation from experimental data. The nonequilibrium model is a 1-temperature, 5-species, 17-reaction model solved by an implicit flux-vector splitting scheme. A loosely coupled approach is implemented to communicate between the magnetogasdynamic equations and the chemistry models. Numerical simulations for steady, inviscid, resistive magnetogasdynamics over a hemisphere subject to a dipole and a circular cylinder–wedge under the influence of an axial magnetic field agree well with existing solutions obtained using different methods. High-temperature effects are investigated for the cylinder configuration at various altitudes and Mach numbers.

Nomenclature

$\boldsymbol{A}$	=	convective flux Jacobian matrix in x direction, associated with $\boldsymbol{E}$
B	=	norm of magnetic field vector, $\|\vec{\boldsymbol{B}}\|$
$\boldsymbol{B}$	=	convective flux Jacobian matrix in y direction, associated with $\boldsymbol{F}$
$\vec{\boldsymbol{B}}$	=	magnetic field vector, $\begin{Bmatrix} B_x \\ B_y \\ B_z \end{Bmatrix}$
$\boldsymbol{C}$	=	convective flux Jacobian matrix in z direction, associated with $\boldsymbol{G}$
c_s	=	mass fraction of species s
$\boldsymbol{E}$	=	convective flux vector in x direction, $\{E\}_{8\times 1}$
$\vec{\boldsymbol{E}}$	=	electric field
$\boldsymbol{E}_v$	=	diffusion flux vector in x direction, $\{E_v\}_{8\times 1}$
e	=	specific internal energy of gas mixture
$e_{e,s}$	=	electronic energy mode of species s
$e_{r,s}$	=	rotational energy mode of species s
e_s	=	specific internal energy of species s
e_t	=	specific total energy of gas mixture
$e_{t,s}$	=	translational energy mode of species s
$e_{v,s}$	=	vibrational energy mode of species s
$\boldsymbol{e}_x, \boldsymbol{e}_y, \boldsymbol{e}_z$	=	Cartesian base unit vectors
$e_{0,s}$	=	zero-point energy of species s
$\boldsymbol{F}$	=	convective flux vector in y direction, $\{F\}_{8\times 1}$
$\boldsymbol{F}_v$	=	diffusion flux vector in y direction, $\{F_v\}_{8\times 1}$
$\boldsymbol{G}$	=	convective flux vector in z direction, $\{G\}_{8\times 1}$
$\boldsymbol{G}_v$	=	diffusion flux vector in z direction, $\{G_v\}_{8\times 1}$
$\boldsymbol{H}$	=	magnetic source flux vector, $\{H\}_{8\times 1}$
h_t	=	specific total enthalpy of gas mixture
$h_{0,s}$	=	specific heat of formation of species s
$\bar{\boldsymbol{I}}$ or $\boldsymbol{I}$	=	identity tensor or identity matrix
J	=	Jacobian of transformation
$\boldsymbol{J}$	=	current density vector
$\boldsymbol{L}$	=	left eigenvector matrix, $\{L\}_{8\times 8}$
M	=	Mach number
p	=	pressure
$\boldsymbol{Q}$	=	solution vector, $\{Q\}_{8\times 1}$
$\boldsymbol{q}$	=	surface heat flux
$\boldsymbol{R}$	=	right eigenvector matrix, $\{R\}_{8\times 8}$
R_b	=	magnetic pressure number
Re	=	Reynolds number
Re_m	=	magnetic Reynolds number
R_s	=	specific gas constant of species s
r_b	=	body radius
$\boldsymbol{S}$	=	electromagnetic source term in low magnetic Reynolds number formulation
T	=	temperature
t	=	time
U	=	norm of velocity vector, $\|\boldsymbol{U}\|$
$\boldsymbol{U}$	=	velocity vector, $\begin{Bmatrix} u \\ v \\ w \end{Bmatrix}$
$\dot{\boldsymbol{W}}_c$	=	mass production/extinction rate flux due to chemical reactions, $\{\dot{w}_c\}_{5\times 5}$
x, y, z	=	Cartesian coordinates
γ	=	ratio of specific heats
Δ	=	shock standoff distance
ζ	=	generalized coordinate
$\zeta_x, \zeta_y, \zeta_z$	=	transformation metrics
η	=	generalized coordinate
η_x, η_y, η_z	=	transformation metrics
$\theta_{v,s}$	=	characteristic vibrational temperature of species s
λ	=	eigenvalue
μ	=	dynamic viscosity
μ_e	=	magnetic permeability
ν_e	=	magnetic diffusivity, $1/\mu_e\sigma_e$
ξ	=	generalized coordinate
ξ_x, ξ_y, ξ_z	=	transformation metrics
ρ	=	density

Received 10 December 2001; revision received 15 April 2002; accepted for publication 15 April 2002.

*Graduate Research Assistant, Department of Aerospace Engineering. Student Member AIAA.

†Professor, Department of Aerospace Engineering. Associate Fellow AIAA.

σ_e = electrical conductivity
$\bar{\bar{\tau}}$ = shear stress tensor
$\bar{\Phi}$ = total variation diminishing (TVD) flux limiter function vector, $\{\bar{\Phi}\}_{8\times 1}$
ψ = entropy correction function in TVD scheme

Subscripts

c = chemical quantity
i = index in ξ direction
j = index in η direction
k = index in ζ direction
ref = reference quantity
SM = number of chemical species
s = index for chemical species
0 = reference quantity or vacuum quantity
∞ = freestream quantity

Superscripts

n = iteration (time) level
$\bar{}$ = quantity expressed in generalized curvilinear coordinates

Introduction

THE design of a cruise hypersonic aircraft remains confronted with the extremely high temperatures experienced in hypervelocity flight. In the conventional approach, thermal protection is provided by heat shields. Furthermore, the nose, wing leading edges, and other segments of hypersonic vehicles that are subject to severe aerodynamic heating are blunt shaped to reduce heat transfer. However, these techniques are not satisfactory for routine hypersonic flight, due to the limitations of the materials constituting the current heat shields and the additional drag associated with detached shock waves over blunt bodies compared to that associated with attached shock waves over sharp configurations.

An alternative to conventional methods is to use magnetic flow control. Indeed, at velocities characteristic of spacecraft reentry, thermal ionization enhances the electrical conductivity of the gas in the shock layers, so that the flow can be influenced by a magnetic field. Magnetogasdynamic (MGD) hypersonic flows over blunt bodies have been the object of intensive investigations since the late 1950s. Some theoretical, semi-analytical and empirical studies are reported in the literature.[1–12] Because the levels of electrical conductivity of thermally ionized air are relatively low, effective magnetic control requires either a strong applied magnetic field or/and enhanced electrical conductivity. This led investigators in the late 1950s and early 1960s, when most of the theoretical, semi-analytical and empirical studies in MGD were conducted, to realize that magnetic flow control was not competitive compared to other types of flow control.[9] Since then, considerable technological progress has taken place in the field of superconducting magnets and enhancement of electrical conductivity by artificial ionization. The present state of the art allows us to reconsider the electromagnetic flow control as an efficient technique for future hypersonic aircraft project such as AJAX.[13,14] A comprehensive literature survey on magnetic flow control is presented in Ref. 15. With the advances in computer technology and development of high-order numerical schemes, computational fluid dynamics (CFD) has emerged and has been extended to magnetofluidynamics. Several numerical schemes have been proposed for the solution of MGD equations and applied to simulations of blunt-body flows.[15–19]

In the hypersonic high-temperature environment, air in the shock layer does not behave as a calorically perfect gas due to chemical reactions. For a calorically perfect gas, the ratio of specific heats γ is constant, and the internal energy e is typically a function of temperature only. For chemically reacting flow, e is a function of both temperature and pressure, and γ is no longer a constant. Three chemical states may be defined, namely, frozen, equilibrium, and nonequilibrium. The determination of the chemical states is based on the relative importance of the following characteristic times: the time for a fluid element to traverse the flowfield of interest, τ_f, and the time for the chemical reactions and/or vibrational energy to approach equilibrium, τ_c. In chemically frozen flow, no chemical reactions take place. In other words, τ_c/τ_f tends to infinity. On the other hand, in chemical equilibrium, reactions are assumed instantaneous, that is, τ_c/τ_f equals zero. Chemical equilibrium may be a good approximation if τ_c is negligible compared to τ_f. In reality, chemical reactions do not take place instantaneously, and τ_c may be of the same order of magnitude as τ_f. In this case, the flow is in chemical nonequilibrium.

Many thermochemical models to simulate high-temperature effects have been proposed by investigators.[20,21] Modeling chemical equilibrium can be accomplished relatively easily by incorporating tables and curve fits of thermodynamic properties.[22] On the other hand, chemical and possible thermal nonequilibrium is more complex due to the abundance of the species present in the medium and the necessity to take into account various energy levels and requires the solution of a set of species conservation equations. Extensions of CFD algorithms to nonequilibrium chemistry have been accomplished by several investigators.[23–25]

The objectives of the present research are to illustrate some features of MGD flows over blunt bodies. Depending on the level of electrical conductivity of the working medium, two different approaches are considered. In the most general case, the system of MGD equations expresses the conservation of mass, momentum, energy, and the magnetic induction. This system is solved by a three-dimensional modified Runge–Kutta scheme augmented with total variation diminishing (TVD) limiters in a postprocessing stage recently developed by the authors.[26] However, when the levels of electrical conductivity are very low, a simpler and more suitable approach is to neglect the induced magnetic field and to solve the gasdynamics equations with magnetic effects represented as a source term. The high-temperature effects on the flow structure and chemical composition are investigated using chemistry models. The governing equations and the numerical schemes are reviewed in the following sections.

Governing Equations

MGD

The full governing equations of magnetogasdynamics can be expressed in a vector form as

$$\frac{\partial}{\partial t}\begin{bmatrix}\rho\\ \rho\boldsymbol{U}\\ \vec{\boldsymbol{B}}\\ \rho e_t\end{bmatrix}+\nabla\cdot\begin{bmatrix}\rho\boldsymbol{U}\\ \rho\boldsymbol{U}\boldsymbol{U}+\left(p+B^2/2\mu_{e0}\right)\bar{\bar{I}}-\vec{\boldsymbol{B}}\vec{\boldsymbol{B}}/\mu_{e0}\\ \boldsymbol{U}\vec{\boldsymbol{B}}-\vec{\boldsymbol{B}}\boldsymbol{U}\\ \left(\rho e_t+p+B^2/2\mu_{e0}\right)\boldsymbol{U}-(\vec{\boldsymbol{B}}/\mu_{e0})(\boldsymbol{U}\cdot\vec{\boldsymbol{B}})\end{bmatrix}$$

$$+\begin{bmatrix}0\\ \vec{\boldsymbol{B}}/\mu_{e0}\\ \boldsymbol{U}\\ \boldsymbol{U}\cdot(\vec{\boldsymbol{B}}/\mu_{e0})\end{bmatrix}\nabla\cdot\vec{\boldsymbol{B}}$$

$$=\begin{bmatrix}0\\ \nabla\cdot\bar{\bar{\tau}}\\ -\nabla\times(\nu_e\nabla\times\vec{\boldsymbol{B}})\\ \nabla\cdot(\bar{\bar{\tau}}\cdot\boldsymbol{U})+\nabla\cdot\boldsymbol{q}+\nu_e\left[(\nabla\times\vec{\boldsymbol{B}})^2/\mu_{e0}\right]\end{bmatrix} \tag{1a}$$

where

$$\rho e_t=\rho(U^2/2)+p/(\gamma-1)+B^2/2\mu_{e0} \tag{1b}$$

The third term in the left-hand side of Eq. (1a), due to the implementation of Powell's scheme,[27] convects numerically induced nonzero divergence of the magnetic field away from the domain of computation. This issue is discussed in detail in Ref. 28.

Equation (1) is valid for continuum, nonrelativistic flows of isotropic, electrically neutral media, with the electromagnetic properties of vacuum. (Magnetic permeability of vacuum is used.) Body

forces other than electromagnetic forces, potential energies, heat due to chemical reactions, and radiation have been neglected.

Theoretically, Eq. (1) describes any MGD phenomenon that meets the assumptions specified earlier. However, for low magnetic Reynolds number flows, Eq. (1) is not suitable for numerical computations, as explained in Ref. 19. Because, for such cases, the applied magnetic field is negligibly disturbed by the flow, the induction equation is dropped. The governing equations are the Navier–Stokes equations amended with a source term representing the electromagnetic effect on the flow written as

$$\frac{\partial}{\partial t}\begin{bmatrix}\rho\\ \rho \boldsymbol{U}\\ \rho e_t\end{bmatrix}+\nabla\cdot\begin{bmatrix}\rho \boldsymbol{U}\\ \rho \boldsymbol{U}\boldsymbol{U}+p\bar{\bar{I}}\\ (\rho e_t+p)\boldsymbol{U}\end{bmatrix}=\begin{bmatrix}0\\ \boldsymbol{J}\times\vec{\boldsymbol{B}}\\ \boldsymbol{J}\cdot\vec{\boldsymbol{E}}\end{bmatrix}+\begin{bmatrix}0\\ \nabla\cdot\bar{\bar{\tau}}\\ \nabla\cdot(\bar{\bar{\tau}}\cdot\boldsymbol{U})+\nabla\cdot\boldsymbol{q}\end{bmatrix} \tag{2a}$$

where

$$\rho e_t=\rho(U^2/2)+p/(\gamma-1) \tag{2b}$$

The current density $\boldsymbol{J}$ is evaluated using Ohm's law as

$$\boldsymbol{J}=\sigma_e(\vec{\boldsymbol{E}}+\boldsymbol{U}\times\vec{\boldsymbol{B}}) \tag{2c}$$

For numerical purposes, Eqs. (1) and (2) are expressed in generalized curvilinear coordinates and nondimensionalized. The high magnetic Reynolds number formulation is

$$\frac{\partial\bar{\boldsymbol{Q}}}{\partial t}+\frac{\partial\bar{\boldsymbol{E}}}{\partial\xi}+\frac{\partial\bar{\boldsymbol{F}}}{\partial\eta}+\frac{\partial\bar{\boldsymbol{G}}}{\partial\zeta}+\bar{\boldsymbol{H}}=\frac{\partial\bar{\boldsymbol{E}}_v}{\partial\xi}+\frac{\partial\bar{\boldsymbol{F}}_v}{\partial\eta}+\frac{\partial\bar{\boldsymbol{G}}_v}{\partial\zeta} \tag{3a}$$

where

$$\bar{\boldsymbol{Q}}=[\rho\quad \rho u\quad \rho v\quad \rho w\quad B_x\quad B_y\quad B_z\quad \rho e_t]^T\big/J \tag{3b}$$

$$\rho e_t=\rho[(u^2+v^2+w^2)/2]+p/(\gamma-1)+\left(B_x^2+B_y^2+B_z^2\right)\big/2 \tag{3c}$$

$\bar{\boldsymbol{E}}$, $\bar{\boldsymbol{F}}$, $\bar{\boldsymbol{G}}$, and $\bar{\boldsymbol{E}}_v$, $\bar{\boldsymbol{F}}_v$, $\bar{\boldsymbol{G}}_v$ represent the convective and diffusion flux terms, respectively. Each flux vector has eight components. The $\bar{\boldsymbol{H}}$ term is the result of the enforcement of Powell's methodology.[27] The low magnetic Reynolds number formulation is

$$\frac{\partial\bar{\boldsymbol{Q}}}{\partial t}+\frac{\partial\bar{\boldsymbol{E}}}{\partial\xi}+\frac{\partial\bar{\boldsymbol{F}}}{\partial\eta}+\frac{\partial\bar{\boldsymbol{G}}}{\partial\zeta}=\frac{\partial\bar{\boldsymbol{E}}_v}{\partial\xi}+\frac{\partial\bar{\boldsymbol{F}}_v}{\partial\eta}+\frac{\partial\bar{\boldsymbol{G}}_v}{\partial\zeta}+\bar{\boldsymbol{S}} \tag{4a}$$

where

$$\bar{\boldsymbol{Q}}=[\rho\quad \rho u\quad \rho v\quad \rho w\quad \rho e_t]^T\big/J \tag{4b}$$

$$\rho e_t=\rho[(u^2+v^2+w^2)/2]+p/(\gamma-1) \tag{4c}$$

In this case, flux vectors $\bar{\boldsymbol{E}}$, $\bar{\boldsymbol{F}}$, $\bar{\boldsymbol{G}}$, and $\bar{\boldsymbol{E}}_v$, $\bar{\boldsymbol{F}}_v$, $\bar{\boldsymbol{G}}_v$ have five components. $\bar{\boldsymbol{S}}$ represents the electromagnetic source term. Details of Eqs. (1–4) are provided in Ref. 28.

Finite-Rate Chemistry Model

The proposed chemistry model is based on thermal dissociations of air molecules:

$$O_2+M\rightleftharpoons 2O+M \tag{5}$$

$$N_2+M\rightleftharpoons 2N+M \tag{6}$$

$$NO+M\rightleftharpoons N+O+M \tag{7}$$

and exchange reactions involving NO:

$$NO+O\rightleftharpoons N+O_2 \tag{8}$$

$$O+N_2\rightleftharpoons N+NO \tag{9}$$

where M is a third body, which can be either O_2, N_2, NO, O, or N. Thus, 17 reactions involving 5 species are considered. The internal specific energy for a species s is expressed for an atom as

$$e_s=e_{t,s}+e_{e,s}+e_{0,s} \tag{10a}$$

and for a molecule as

$$e_s=e_{t,s}+e_{r,s}+e_{v,s}+e_{e,s}+e_{0,s} \tag{10b}$$

where $e_{t,s}$, $e_{r,s}$, $e_{v,s}$, $e_{e,s}$, and $e_{0,s}$ represent the translational, rotational, vibrational, electronic, and zero-point specific energies, respectively. Statistical thermodynamics leads to the following expressions:

$$e_{t,s}=\tfrac{3}{2}R_sT \tag{11a}$$

$$e_{r,s}=R_sT \tag{11b}$$

$$e_{v,s}=\frac{\theta_{v,s}/T}{\exp(\theta_{v,s}/T)-1}R_sT \tag{11c}$$

In this model, the electronic energy is neglected. For air, neglecting this energy is a reasonable assumption, which induces an error less than 1% (Ref. 23). The zero-point energy is replaced by the heat of formation $h_{0,s}$. Thus, the internal specific energy for an atom is rewritten as

$$e_s=\tfrac{3}{2}R_sT+h_{0,s} \tag{12a}$$

and for a diatomic molecule is

$$e_s=\frac{3}{2}R_sT+R_sT+\frac{R_s\theta_{v,s}}{\exp(\theta_{v,s}/T)-1}+h_{0,s} \tag{12b}$$

The continuity equation for the chemical species is expressed in a flux-vector form as

$$\frac{\partial\bar{\boldsymbol{Q}}_c}{\partial t_c}+\frac{\partial\bar{\boldsymbol{E}}_c}{\partial\xi}+\frac{\partial\bar{\boldsymbol{F}}_c}{\partial\eta}+\frac{\partial\bar{\boldsymbol{G}}_c}{\partial\zeta}=\bar{\dot{\boldsymbol{W}}}_c \tag{13a}$$

where the chemical solution vector is

$$\bar{\boldsymbol{Q}}_c=[\rho c_1\quad \rho c_2\quad \rho c_3\quad \cdots\quad \rho c_{SM}]^T\big/J \tag{13b}$$

$\bar{\boldsymbol{E}}_c$, $\bar{\boldsymbol{F}}_c$, $\bar{\boldsymbol{G}}_c$ denote the convective flux terms for the chemical species. The $\bar{\dot{\boldsymbol{W}}}_c$ term, representing the rate of production or extinction of the chemical species due to chemical reactions, is evaluated using chemical kinetics. Details of Eq. (13) are provided in Ref. 28.

Numerical Methods

Modified Runge–Kutta Scheme

The MGD equations are solved using a four-stage modified Runge–Kutta scheme amended with a TVD scheme (RK4TVD) as follows. For the maximum index in the ξ direction (IM), the maximum index in the η direction (JM), and the maximum index in the ζ direction (KM):

$$\forall i\in\{2,\mathrm{IM}-1\},\qquad \forall j\in\{2,\mathrm{JM}-1\}$$

$$\forall k\in\{2,\mathrm{KM}-1\},\qquad \bar{\boldsymbol{Q}}^{(0)}_{i,j,k}=\bar{\boldsymbol{Q}}^{n}_{i,j,k} \tag{14a}$$

The four stages are

$$\bar{\boldsymbol{Q}}^{(1)}_{i,j,k} = \bar{\boldsymbol{Q}}^{n}_{i,j,k} - (\Delta t/4)\bar{\boldsymbol{f}}^{(0)}_{i,j,k} \tag{14b}$$

$$\bar{\boldsymbol{Q}}^{(2)}_{i,j,k} = \bar{\boldsymbol{Q}}^{n}_{i,j,k} - (\Delta t/3)\bar{\boldsymbol{f}}^{(1)}_{i,j,k} \tag{14c}$$

$$\bar{\boldsymbol{Q}}^{(3)}_{i,j,k} = \bar{\boldsymbol{Q}}^{n}_{i,j,k} - (\Delta t/2)\bar{\boldsymbol{f}}^{(2)}_{i,j,k} \tag{14d}$$

$$\bar{\boldsymbol{Q}}^{(4)}_{i,j,k} = \bar{\boldsymbol{Q}}^{n}_{i,j,k} - \Delta t\bar{\boldsymbol{f}}^{(3)}_{i,j,k} \tag{14e}$$

where, for the high Reynolds number Re_m formulation,

$$\bar{\boldsymbol{f}} = \frac{\partial \bar{\boldsymbol{E}}}{\partial \xi} + \frac{\partial \bar{\boldsymbol{F}}}{\partial \eta} + \frac{\partial \bar{\boldsymbol{G}}}{\partial \zeta} + \bar{\boldsymbol{H}} - \frac{\partial \bar{\boldsymbol{E}}_v}{\partial \xi} - \frac{\partial \bar{\boldsymbol{F}}_v}{\partial \eta} - \frac{\partial \bar{\boldsymbol{G}}_v}{\partial \zeta}$$

and, for the low Reynolds number Re_m formulation,

$$\bar{\boldsymbol{f}} = \frac{\partial \bar{\boldsymbol{E}}}{\partial \xi} + \frac{\partial \bar{\boldsymbol{F}}}{\partial \eta} + \frac{\partial \bar{\boldsymbol{G}}}{\partial \zeta} - \frac{\partial \bar{\boldsymbol{E}}_v}{\partial \xi} - \frac{\partial \bar{\boldsymbol{F}}_v}{\partial \eta} - \frac{\partial \bar{\boldsymbol{G}}_v}{\partial \zeta} - \bar{\boldsymbol{S}}$$

The postprocessing stage is

$$\begin{aligned}\bar{\boldsymbol{Q}}^{n+1}_{i,j,k} = \bar{\boldsymbol{Q}}^{(4)}_{i,j,k} &- \tfrac{1}{2}(\Delta t/\Delta\xi)\Big[(\bar{\boldsymbol{R}}_\xi)^n_{i+\frac{1}{2},j,k}(\bar{\Phi}_\xi)^n_{i+\frac{1}{2},j,k} \\ &- (\bar{\boldsymbol{R}}_\xi)^n_{i-\frac{1}{2},j,k}(\bar{\Phi}_\xi)^n_{i-\frac{1}{2},j,k}\Big] \\ &- \tfrac{1}{2}(\Delta t/\Delta\eta)\Big[(\bar{\boldsymbol{R}}_\eta)^n_{i,j+\frac{1}{2},k}(\bar{\Phi}_\eta)^n_{i,j+\frac{1}{2},k} \\ &- (\bar{\boldsymbol{R}}_\eta)^n_{i,j-\frac{1}{2},k}(\bar{\Phi}_\eta)^n_{i,j-\frac{1}{2},k}\Big] \\ &- \tfrac{1}{2}(\Delta t/\Delta\zeta)\Big[(\bar{\boldsymbol{R}}_\zeta)^n_{i,j,k+\frac{1}{2}}(\bar{\Phi}_\zeta)^n_{i,j,k+\frac{1}{2}} \\ &- (\bar{\boldsymbol{R}}_\zeta)^n_{i,j,k-\frac{1}{2}}(\bar{\Phi}_\zeta)^n_{i,j,k-\frac{1}{2}}\Big]\end{aligned} \tag{14f}$$

The convective and diffusion terms are evaluated using second-order central finite differences. The Davis–Yee symmetric second-order TVD scheme is implemented. Details of Eq. (14) are provided in Ref. 28.

Implicit Flux-Vector Splitting

The continuity equation for the chemical species is solved by an implicit flux-vector splitting scheme as shown next for the two-dimensional case:

$$\lambda_{c\xi} \geq \boldsymbol{0} \Rightarrow \begin{cases} \bar{\boldsymbol{A}}^+_c = \bar{\boldsymbol{A}}_c, & \bar{\boldsymbol{A}}^-_c = \boldsymbol{0} \\ \bar{\boldsymbol{E}}^+_c = \bar{\boldsymbol{E}}_c, & \bar{\boldsymbol{E}}^-_c = \boldsymbol{0} \end{cases}$$

$$\lambda_{c\xi} < \boldsymbol{0} \Rightarrow \begin{cases} \bar{\boldsymbol{A}}^+_c = \boldsymbol{0}, & \bar{\boldsymbol{A}}^-_c = \bar{\boldsymbol{A}}_c \\ \bar{\boldsymbol{E}}^+_c = \boldsymbol{0}, & \bar{\boldsymbol{E}}^-_c = \bar{\boldsymbol{E}}_c \end{cases} \tag{15a}$$

$$\lambda_{c\eta} \geq \boldsymbol{0} \Rightarrow \begin{cases} \bar{\boldsymbol{B}}^+_c = \bar{\boldsymbol{B}}_c, & \bar{\boldsymbol{B}}^-_c = \boldsymbol{0} \\ \bar{\boldsymbol{F}}^+_c = \bar{\boldsymbol{F}}_c, & \bar{\boldsymbol{F}}^-_c = \boldsymbol{0} \end{cases}$$

$$\lambda_{c\eta} < \boldsymbol{0} \Rightarrow \begin{cases} \bar{\boldsymbol{B}}^+_c = \boldsymbol{0}, & \bar{\boldsymbol{B}}^-_c = \bar{\boldsymbol{B}}_c \\ \bar{\boldsymbol{F}}^+_c = \boldsymbol{0}, & \bar{\boldsymbol{F}}^-_c = \bar{\boldsymbol{F}}_c \end{cases} \tag{15b}$$

When first-order finite differences are used, the flux-split form of Eq. (13) for the chemical auxiliary (CA) matrices CAM, CAP, CBM, and CBP is

$$\begin{aligned}&\mathrm{CAM}_{i,j}\Delta\bar{\boldsymbol{Q}}_{ci-1,j} + \mathrm{CAP}_{i,j}\Delta\bar{\boldsymbol{Q}}_{ci+1,j} + \mathrm{CBM}_{i,j}\Delta\bar{\boldsymbol{Q}}_{ci,j-1} \\ &+ \mathrm{CBP}_{i,j}\Delta\bar{\boldsymbol{Q}}_{ci,j+1} + \Big[\boldsymbol{I} + (\Delta t_c/\Delta\xi)\big(\bar{\boldsymbol{A}}^+_{ci,j} - \bar{\boldsymbol{A}}^-_{ci,j}\big)^n \\ &+ (\Delta t_c/\Delta\eta)\big(\bar{\boldsymbol{B}}^+_{ci,j} - \bar{\boldsymbol{B}}^-_{ci,j}\big)^n - \Delta t_c\bar{\boldsymbol{D}}^n_{ci,j}\Big]\Delta\bar{\boldsymbol{Q}}_{ci,j} = \mathrm{RHS}_{i,j}\end{aligned} \tag{16}$$

where

$$\mathrm{CAM}_{i,j} = -(\Delta t_c/\Delta\xi)\big(\bar{\boldsymbol{A}}^+_{ci-1,j}\big)^n \tag{17a}$$

$$\mathrm{CAP}_{i,j} = (\Delta t_c/\Delta\xi)\big(\bar{\boldsymbol{A}}^-_{ci+1,j}\big)^n \tag{17b}$$

$$\mathrm{CBM}_{i,j} = -(\Delta t_c/\Delta\eta)\big(\bar{\boldsymbol{B}}^+_{ci,j-1}\big)^n \tag{17c}$$

$$\mathrm{CBP}_{i,j} = (\Delta t_c/\Delta\eta)\big(\bar{\boldsymbol{B}}^-_{ci,j+1}\big)^n \tag{17d}$$

and the right-hand side (RHS) is as follows:

$$\begin{aligned}\mathrm{RHS}_{i,j} = -\Big[&(\Delta t_c/\Delta\xi)\big(\bar{\boldsymbol{E}}^+_{ci,j} - \bar{\boldsymbol{E}}^+_{ci-1,j} + \bar{\boldsymbol{E}}^-_{ci+1,j} - \bar{\boldsymbol{E}}^-_{ci,j}\big)^n \\ &+ (\Delta t_c/\Delta\xi)\big(\bar{\boldsymbol{F}}^+_{ci,j} - \bar{\boldsymbol{F}}^+_{ci,j-1} + \bar{\boldsymbol{F}}^-_{ci,j+1} - \bar{\boldsymbol{F}}^-_{ci,j}\big)^n - \Delta t_c\bar{\dot{\boldsymbol{W}}}^n_{ci,j}\Big]\end{aligned} \tag{17e}$$

This implicit formulation results in a pentadiagonal system, the solution of which is computationally time consuming. To alleviate this problem, an approximate factorization is introduced to reduce the pentadiagonal matrix system into two tridiagonal matrix systems for which efficient solution procedures exist, as follows:

$$\forall i \in \{2, IM-1\}, \qquad \forall j \in \{2, JM-1\}$$

$$\mathrm{CBM}_{i,j}\Delta\bar{\boldsymbol{Q}}'_{ci,j-1} + \mathrm{CB}_{i,j}\Delta\bar{\boldsymbol{Q}}'_{ci,j} + \mathrm{CBP}_{i,j}\Delta\bar{\boldsymbol{Q}}'_{ci,j+1} = \mathrm{RHS}_{i,j} \tag{18}$$

$$\mathrm{CAM}_{i,j}\Delta\bar{\boldsymbol{Q}}_{ci-1,j} + \mathrm{CA}_{i,j}\Delta\bar{\boldsymbol{Q}}_{ci,j} + \mathrm{CAP}_{i,j}\Delta\bar{\boldsymbol{Q}}_{ci+1,j} = \Delta\bar{\boldsymbol{Q}}'_{ci,j} \tag{19}$$

where

$$\mathrm{CA}_{i,j} = \boldsymbol{I} + (\Delta t_c/\Delta\xi)\big(\bar{\boldsymbol{A}}^+_{ci,j} - \bar{\boldsymbol{A}}^-_{ci,j}\big)^n \tag{20a}$$

$$\mathrm{CB}_{i,j} = \boldsymbol{I} + (\Delta t_c/\Delta\eta)\big(\bar{\boldsymbol{B}}^+_{ci,j} - \bar{\boldsymbol{B}}^-_{ci,j}\big)^n - \Delta t_c\bar{\boldsymbol{D}}^n_{ci,j} \tag{20b}$$

Given $\mathrm{RHS}_{i,j}$, Eq. (18) can be solved for $\Delta\bar{\boldsymbol{Q}}'_{ci,j}$, which provides the RHS of Eq. (19) that is subsequently solved for $\Delta\bar{\boldsymbol{Q}}_{ci,j}$. Details of the flux-splitting scheme are provided in Ref. 28.

Loosely Coupled Scheme

Physically, fluid dynamics and chemical reactions are intrinsically coupled. Thus, solving both systems of equations simultaneously is a logical procedure, called the "coupled method." If such an approach were selected, a modification of the flux vectors and the flux Jacobian matrices associated with the MGD governing equations would be required to account for the mass conservation of the chemical species. This would result in a large system of equations, and the system eigenstructure (used in the TVD scheme) would have to be determined. A simpler and more efficient approach, known as the "loosely coupled method," is to solve the MGD equations and chemistry equations separately in an iterative fashion. The integration of the loosely coupled scheme is described by the following steps. (1) The MGD equations are solved for the conservative variable $\bar{\boldsymbol{Q}}$ by the RK4TVD scheme. At this step, the chemical mass fractions, the ratio of specific heats, and the gas constant of the mixture are held to their previous values. (2) Based on $\bar{\boldsymbol{Q}}$, the rate of mass change of chemical species $\bar{\dot{\boldsymbol{W}}}_c$ is evaluated, and Eq. (13) is solved for the chemical variable $\bar{\boldsymbol{Q}}_c$. Subsequently, the mixture gas constant is updated. (3) System temperature, that is, translational temperature is determined using a one-temperature model. (4) Finally, all of the remaining flow properties can be updated. Steps 1–4 are repeated until a convergence criterion is satisfied.

Validation Cases

To evaluate the performance of the numerical code, several test cases are considered, for which either analytical solutions or numerical solutions obtained with different methods are available. First, the solution scheme in the low magnetic Reynolds number formulation

is validated for hypersonic flow over a hemisphere, by comparison to analytical and numerical solutions reported in the literature. Second, the accuracy of the scheme in the high magnetic Reynolds formulation is demonstrated by solving the MGD flow over a cylinder. Finally, the finite-rate chemistry model is investigated.

Note that the values of electrical conductivity used in the current research are selected to achieve similarity with other solutions reported in the literature, for validation purposes. High-temperature effects on the electrical conductivity have not been considered.

Hypersonic Flow over A Hemisphere in the Low Magnetic Reynolds Number Approximation

To validate the scheme in the low magnetic Reynolds number formulation, the flow over a hemisphere in the presence of a dipole located at its center is simulated. In an attempt to reproduce the results obtained analytically by Bush[3] and Coakley and Porter,[12] the following assumptions are imposed. Air is a calorically perfect gas, and the flow is laminar. The electrical conductivity is set to zero in the freestream and to a finite value in the postshock region. The dipole distribution is specified in the entire domain of computation. Freestream conditions are used at the inflow. A zero-order extrapolation scheme is utilized for all primitive variables at the outflow. At the solid surface, the slip velocity condition, zero normal gradient of the sum of static and magnetic pressures, and zero normal temperature gradient are enforced. For the purpose of comparison with Poggie and Gaitonde's solutions,[15] computations are performed for a freestream Mach number $M_{\text{ref}} = 5$ and magnetic Reynolds number $Re_{m\,\text{ref}} = 0.01$. The computational mesh is shown in Fig. 1, and selected magnetic field lines of dipole are shown in Fig. 2. The application of a strong magnetic field leads to an increase in the shock standoff distance, as shown in Fig. 3. The comparison of the shock standoff distance of the present simulation with other investigators' results, extracted from Ref. 15, is shown in Fig. 4. The present computations coincide almost perfectly with Poggie and Gaitonde's predictions. Both Bush's theory[3] and Coakley and Porter's[12] results underestimate the shock standoff distance; however, the predictions of the latter are closer to the numerical solutions. The relative error between Bush's solution[3] and the present numerical simulation increases from 13% for $Q_{\text{ref}} = 0$ up to 27% for $Q_{\text{ref}} = 6$, where $Q = \sigma_e B^2 L/\rho U$. Poggie and Gaitonde[15] attribute the difference observed between the numerical simulations and Bush's solution[3] to the constant-density theory on which the latter solution is based. In this theory, the hypersonic shock layer near the body nose is assumed incompressible because the Mach number in this region is low. Such an approximation is not well verified, and it is not implemented in the present numerical algorithm. Nevertheless, this theory provides reasonable results in the case of large shock density ratios. In the absence of an applied electric field, the magnetic force has a decelerating effect. The reduction in the stagnation-point velocity gradient is shown in Fig. 5. The current numerical solution falls between the values predicted by Bush's theory[3] and Poggie and Gaitonde's solution.[15] However, an excellent agreement in the trend is obtained.

The present computations were conducted for a density ratio of $\rho_2/\rho_1 \approx 5$. Now, a ratio of specific heats of 1.2 is selected, which leads to a density ratio of $\rho_2/\rho_1 \approx 7.9$. The shock standoff distance computed in this condition is presented in Fig. 6. Again, the present numerical solution matches almost exactly Poggie and Gaitonde's solution[15] and is also in relative agreement with Bush's theory.[3] (Relative error between Bush's solution and the present numerical simulation is 9% for $Q_{\text{ref}} = 0$ and 23% for $Q_{\text{ref}} = 6$.)

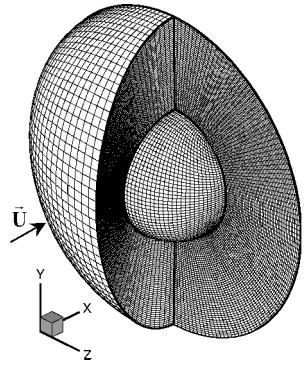

Fig. 1 Mesh for the hemisphere consisting of 50 × 50 × 50 grid points (cutaway plot).

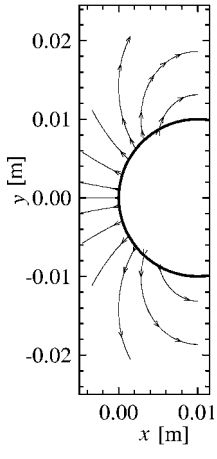

Fig. 2 Imposed dipolar magnetic field on the hemisphere.

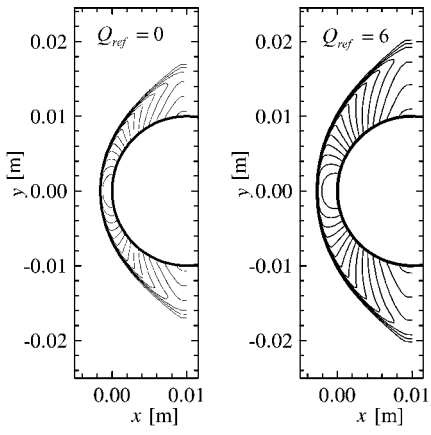

Fig. 3 Effect of magnetic field on the pressure field over the hemisphere for $M_{\text{ref}} = 5$, $Re_{m\,\text{ref}} = 0.01$, and $\gamma = 1.4$.

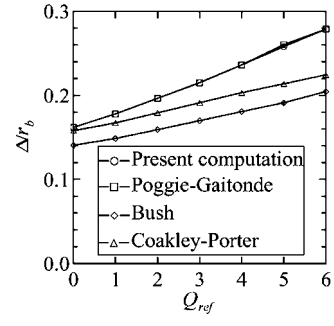

Fig. 4 Effect of applied magnetic field on shock standoff distance, $\gamma = 1.4$.

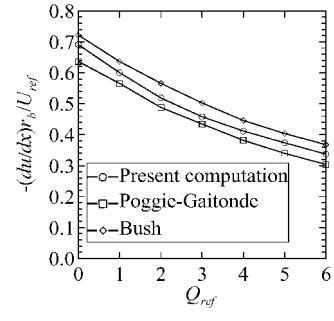

Fig. 5 Effect of applied magnetic field on the stagnation point velocity gradient, $\gamma = 1.4$.

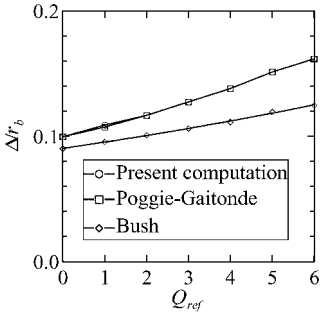

Fig. 6 Effect of applied magnetic field on shock standoff distance, $\gamma = 1.2$.

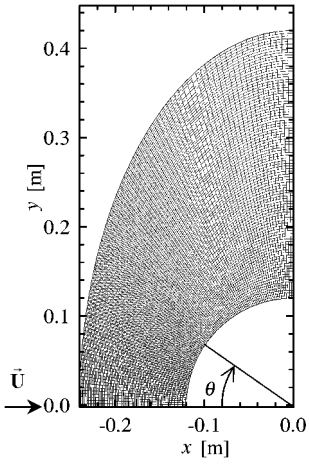

Fig. 7 Mesh for the cylinder consisting of 100 × 100 × 3 grid points.

Hypersonic Flow over a Cylinder in the High Magnetic Reynolds Number Formulation

The performance of the scheme in the solution of the MGD equations expressed in the high Reynolds number formulation is investigated for hypersonic flow over a circular cylinder–wedge body. For the purpose of validation, the setup of the present problem is chosen to mimic Gaitonde and Poggie's simulations.[19] A magnetic field oriented in the z direction is imposed uniformly at the body surface, and no electric field is applied. The freestream velocity vector points in the positive x direction. Because the MGD flowfield is expected to be symmetrical about the (x, z) plane, computations are performed in the half-plane $(x, y \geq 0)$ for efficiency purposes. Figure 7 shows the mesh consisting of $100 \times 100 \times 3$ grid points.

For symmetry about the x axis, reflexive boundary conditions along the $i = 1$ line (which is just below the x axis) are specified. Freestream conditions and zero magnetic field are specified at the inflow. Zero-order extrapolation for all primitive variables is used for the outflow. At the solid surface, the slip velocity condition, zero normal gradient of the sum of static and magnetic pressures, zero normal temperature gradient, and uniform value of magnetic field are specified.

Note that the present case skirts the issue of numerically induced nonzero divergence of magnetic field. Indeed, for a two-dimensional flow, a magnetic field orthogonal to the plane of the flow is mathematically divergence free. Note that a fixed strength of magnetic field is assumed at the body surface. In reality, the magnetic induction at the surface would modify the imposed field as first pointed out by Porter and Cambel.[29] This phenomenon is not addressed in this investigation.

The effect of the magnetic pressure number $R_{b\,\mathrm{ref}}(R_b = B^2/\rho\mu_e U^2)$ is numerically investigated, for a Mach number $M_{\mathrm{ref}} = 16$ and a magnetic Reynolds number $Re_{m\,\mathrm{ref}} = 12.5$. The pressure field in the presence and absence of magnetic field is shown in Fig. 8. As expected, the shock wave moves upstream as the applied magnetic field is increased. For the magnetic case, the inclined contours lines at the body surface suggest that the normal gradient of static pressure is not zero, as it is for the nonmagnetic case. The profiles of static pressure along the stagnation streamline, presented in Fig. 9, confirm that the normal static pressure gradient is indeed not zero if a magnetic field is applied at the wall. It is also observed that surface pressure decreases with increasing magnetic field. Comparison of the present simulation with solution reported in Ref. 19 shows good agreement. Because of the use of a relatively fine mesh, the present simulation yields a superior resolution of the shock wave. For the case $R_{b\,\mathrm{ref}} = 1.0$, the magnetic field is attenuated at the shoulder to prevent the occurrence of negative static pressure. In the current investigation, the applied magnetic field at the surface is decreased linearly to zero in the streamwise direction from $\theta = 63.5$ to 90 deg, which may differ from the attenuation used in Ref. 19. This would explain the discrepancy in the shock standoff distance. However, pressure compares well. As a reference, Billig's correlation[30] for the shock standoff distance in the absence of magnetic field is also provided, which shows excellent agreement with the numerical simulations. Figure 9b shows the variation of temperature along the stagnation streamline. The magnetic field, imposed at the body surface, tends to reduce the surface temperature, although a rise in temperature occurs in a region near the body surface, due to the joule dissipation. For comparison purpose, the temperature profile without joule heating is also provided for the case $R_{b\,\mathrm{ref}} = 0.5$. When joule heating is omitted, no peak in temperature occurs. It is also observed that the shock standoff is dramatically reduced. Figure 10 shows the variation of total pressure along the stagnation streamline. The total pressure is defined as the sum of the static, dynamic, and magnetic pressures. The present results compare well with those

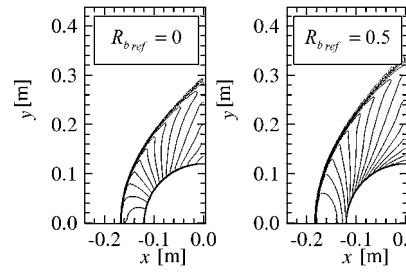

Fig. 8 Effect of magnetic field on the flow over the cylinder; pressure contours for $M_{\mathrm{ref}} = 16$ and $Re_{m\,\mathrm{ref}} = 12.5$.

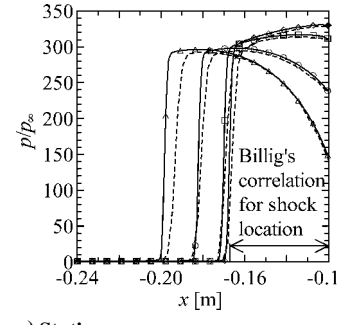

a) Static pressure

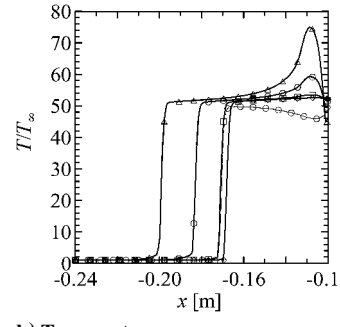

b) Temperature

Fig. 9 Effect of magnetic field on the flow over the cylinder; profiles of static pressure and temperature along the stagnation streamline: ——, present computation; – – –, Gaitonde–Poggie[19]; ♦, analytical; ○, without joule heating; ◇, $R_{b\,\mathrm{ref}} = 0.0$; □, $R_{b\,\mathrm{ref}} = 0.1$; ○, $R_{b\,\mathrm{ref}} = 0.5$; and △, $R_{b\,\mathrm{ref}} = 1.0$.

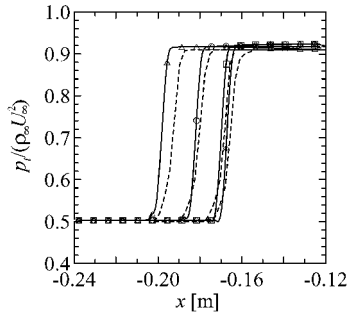

Fig. 10 Effect of magnetic field on the flow over the cylinder; profiles of total pressure along the stagnation streamline: ——, present computation; – – –, Gaitonde–Poggie[19]; ◇, $R_{b\,\mathrm{ref}} = 0.0$; □, $R_{b\,\mathrm{ref}} = 0.1$; ○, $R_{b\,\mathrm{ref}} = 0.5$; and △, $R_{b\,\mathrm{ref}} = 1.0$.

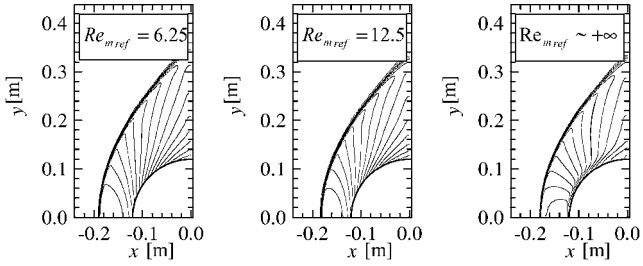

a) Pressure field

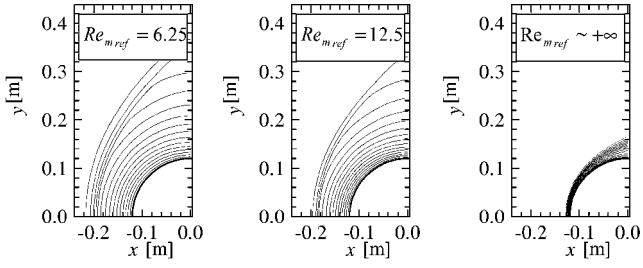

b) Axial magnetic field

Fig. 11 Effect of magnetic Reynolds number on the flow over the cylinder; pressure and magnetic field contours for $M_{\mathrm{ref}} = 16$ and $R_{b\,\mathrm{ref}} = 0.5$.

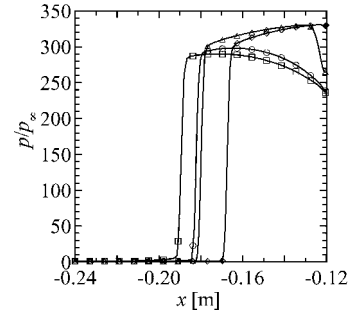

Static pressure

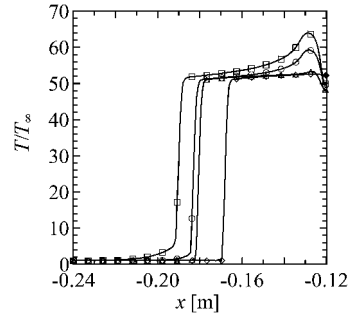

Temperature

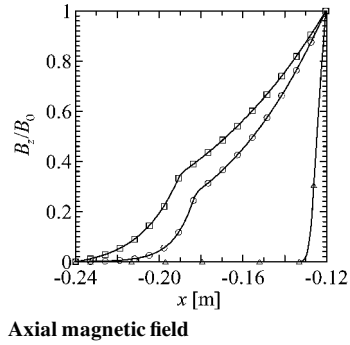

Axial magnetic field

Fig. 12 Effect of magnetic Reynolds number on the flow over the cylinder; profiles of static pressure, temperature, and axial magnetic field along the stagnation streamline: ◇, nonmagnetic; ♦, analytical; □, $Re_{m\,\mathrm{ref}} = 6.25$; ○, $Re_{m\,\mathrm{ref}} = 12.50$; and △, $Re_{m\,\mathrm{ref}} = +\infty$.

reported in Ref. 19. Although static pressure decreases with magnetic field, no clear effect on the total pressure is observed, which suggests no reduction in wave drag.

The effect of magnetic diffusion is now examined by varying the magnetic Reynolds number $Re_{m\,\mathrm{ref}}$ for a Mach number $M_{\mathrm{ref}} = 16$ and a magnetic pressure number $R_{b\,\mathrm{ref}} = 0.5$. Values of Reynolds number $Re_{m\,\mathrm{ref}}$ are varied via the electrical conductivity. Note that this series of experiments is conducted with the full MGD equations, which prohibits the use of zero or very small values of Reynolds number $Re_{m\,\mathrm{ref}}$. For a magnetic Reynolds number equal to zero, that is, for perfectly electrical insulating fluid, no magnetic interaction is expected. Figure 11 shows the effect of the magnetic Reynolds number on the pressure field and the magnetic field. The shock standoff distance is greatly affected by the magnetic Reynolds number: The higher the magnetic Reynolds number is, the closer the shock wave to the body. Figure 11b provides some clues to better understand this phenomenon. As the magnetic Reynolds number is increased, the magnetic field permeates the fluid less and less freely. Eventually, for the perfectly conducting fluid, that is, for $Re_{m\,\mathrm{ref}} \sim +\infty$, the magnetic field is rigidly coupled with the flow and is convected by fluid particles.

The variation of selected flow variables along the stagnation streamline is presented in Fig. 12. For finite nonzero magnetic Reynolds number, the flow undergoes a smooth expansion in the postshock region. In contrast, for infinite magnetic Reynolds number, a relatively sharp expansion is observed near the body surface. Temperature is also greatly affected due to joule heating. The higher the magnetic Reynolds number is, the lower the peak in temperature near the body surface. Theoretically, for infinite magnetic Reynolds number, the magnetic field is trapped at the surface, where it is imposed. However, because of the artificial viscosity inherent in the numerical scheme and because of the mesh definition, the magnetic field is slightly smeared at the surface. Nonetheless, the magnetic field is confined at the body surface, where its interaction with the fluid is maximal.

Hypersonic Chemistry for Flow over a Cylinder

In this series of numerical experiments, high-temperature effects on hypersonic flow over a circular cylinder–wedge are explored at various altitudes and Mach numbers. The setup of this problem is the same as in the preceding section, except that the magnetic field applied at the body surface is not uniform, but follows the relation $B_z = B_0 \cos\theta$, where θ is the angle between the x axis and a point on the body surface and B_0 is the magnetic field strength at the stagnation point. To reduce computation time, a two-dimensional version of the numerical code is utilized with the mesh shown in Fig. 13. For initialization of nonequilibrium simulations, frozen flow computations are performed until a transient detached shock wave forms in front of the body. Subsequently, the nonequilibrium model is switched on. Nondissociated air (23.5% of O_2 and 76.5% of N_2) is considered for the specification of initial mass fractions. The wall is assumed noncatalytic.

To validate of the finite-rate chemistry model, a Mach 18 flow, at an altitude of 30 km is computed and compared to the solution in chemical equilibrium. Under such conditions, the flow is expected to be roughly in chemical equilibrium in the postshock region, where density and temperature are high. Figure 14 compares selected flow variables along the stagnation streamline in various chemical states.

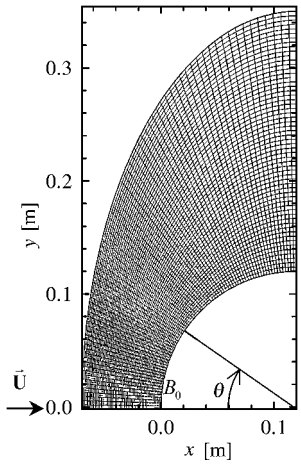

Fig. 13 Mesh for simulation of high-temperature effects on the flow over the cylinder, consisting of 60 × 80 grid points.

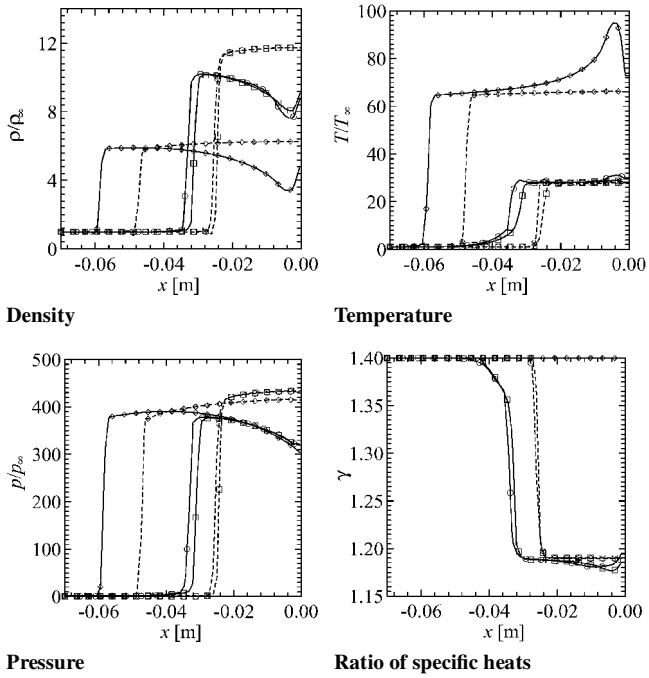

Fig. 14 Comparison of chemical models for flow over the cylinder for $M_{\text{ref}} = 18$ and $Re_{m\,\text{ref}} = 12.5$, at an altitude of 30 km; flow variables along the stagnation streamline: – – –, $R_{b\,\text{ref}} = 0$; ——, $R_{b\,\text{ref}} = 0.5$; ◇, frozen; □, equilibrium; and ○, nonequilibrium.

The frozen flow model yields values of density and temperature, which are off by a factor of two compared to the chemically reacting flow values. All models predict a similar level of postshock pressure. As expected, under the current conditions, the equilibrium and nonequilibrium models lead to nearly identical solutions. However, the small peak in temperature immediately downstream of the shock wave reveals that nonequilibrium features are still present in the flow. As a result, the shock standoff distance in nonequilibrium is slightly larger than in equilibrium.

Figure 15 shows the relative variations of the chemical mass fractions with distance along the stagnation streamline. In the postshock region, diatomics O_2 and N_2 dissociate, the dissociation of O_2 being the most important. As expected, the mass fractions of O and N increase, rising from their frozen flow values (essentially zero) ahead of the shock wave and tending to their equilibrium values farther downstream. For the nonmagnetic case, in which the postshock flow variables (density, pressure, temperature, etc.) are quasi uniform along the stagnation streamline, nonequilibrium mass fractions of all chemical species, except nitric oxide NO, range between the two extremes of frozen and equilibrium values. For the magnetic case, the species mass fractions may exceed the two extremes of frozen and equilibrium values. For instance, in the region of considerable joule heating, a larger amount of O_2 and N_2 is dissociated, compared to the nonmagnetic case.

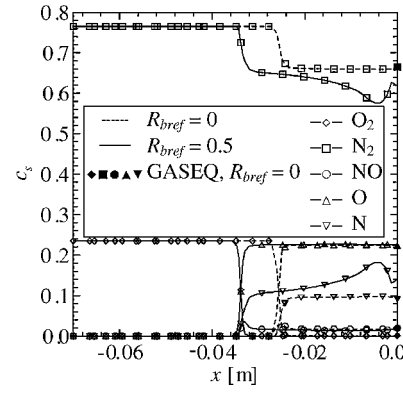

Fig. 15 Relative distribution of chemical mass fractions along the stagnation streamline in chemical nonequilibrium for $M_{\text{ref}} = 18$ and $Re_{m\,\text{ref}} = 12.5$, at an altitude of 30 km.

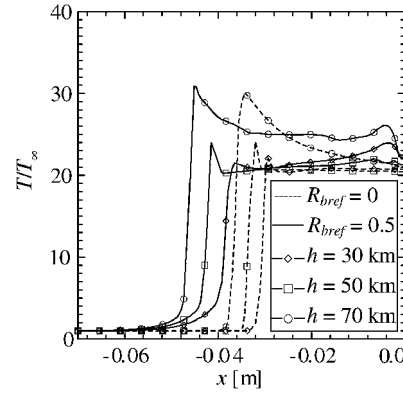

Fig. 16 Effect of altitude on the flow over the cylinder at Mach 14; temperature along the stagnation streamline in chemical nonequilibrium.

The NO overshoot observed immediately downstream of the shock wave may be explained based on the arguments reported in Refs. 31 and 32 as follows. Downstream of the shock wave, diatomics O_2 and N_2 dissociate, which releases O atoms and N atoms. The production of O atoms triggers the NO exchange reactions $O + N_2 \rightleftharpoons N + NO$ and $N + O_2 \rightleftharpoons O + NO$. These reactions are extremely fast, and they rapidly lead to a local equilibrium expressed as $O_2 + N_2 \rightleftharpoons 2NO$. The net effect of these two reactions is to convert N_2 and O_2 into NO. Because the reactions are very fast, an excess of NO is produced immediately downstream of the shock wave, where there is plenty of O_2 and N_2. As O_2 continues to dissociate (farther downstream of the shock wave), the shuffle reactions are reversed, and nitric oxide NO is reduced toward its final value by this means as well as by direct dissociation.

As a measure of validation of the present effort, equilibrium mass fractions computed behind a normal shock wave by GASEQ, a program based on a NASA algorithm,[33] are provided, which show a good agreement with the current solution at the stagnation point. Indeed, along the stagnation streamline, a fluid element is decelerated and comes to a stop at the stagnation point, where chemical reactions have time to reach equilibrium.

The effect of altitude on the flow structure and chemical composition is investigated by changing the flow properties (pressure, density, temperature, etc.) according to the U.S. standard atmosphere model. Altitude is varied in the range 30–70 km with all reference similarity parameters set as $M_{\text{ref}} = 14$, $R_{b\,\text{ref}} = 0.5$, and $Re_{m\,\text{ref}} = 12.5$.

Figure 16 shows the temperature profiles along the stagnation streamline at various altitudes. The peak immediately downstream of the shock wave, which becomes more pronounced as altitude is increased, reveals a region of nonequilibrium. Roughly speaking, at

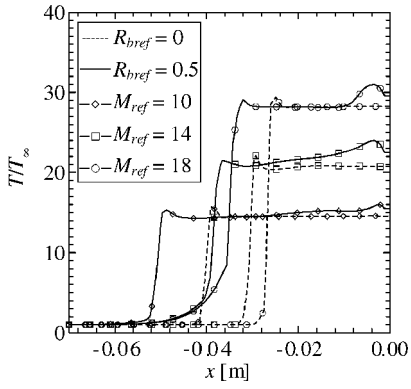

Fig. 17 Effect of Mach number on the flow over the cylinder at an altitude of 30 km; temperature along the stagnation streamline in chemical nonequilibrium.

low altitudes, near chemical equilibrium exists, whereas, at higher altitudes, nonequilibrium phenomena dominate the flowfield.

Next, the effect of Mach number on the solution is considered. To isolate the effect of this parameter, altitude is fixed at 30 km, and magnetic similarity parameters are set to $R_{b\,\mathrm{ref}} = 0.5$ and $Re_{m\,\mathrm{ref}} = 12.5$. Figure 17 shows the temperature profiles along the stagnation streamline at various Mach numbers. At a given altitude, the postshock temperature increases with the Mach number, which enhances the chemical kinetics. The higher the Mach number is, the faster the flow approaches chemical equilibrium. However, at a given altitude, higher Mach number translates into higher velocity. If the fluid particles cross the shock wave in a time smaller than the time required for the chemical reactions, the flow immediately behind the shock wave is in chemical nonequilibrium, as revealed by the peak in temperature, observed for all Mach numbers.

Conclusions

Numerical studies of hypersonic flows over blunt bodies were carried out to investigate the possibility of magnetic flow control. The numerical scheme selected for the solution of the governing equations of MGD is a four-stage modified Runge–Kutta with TVD limiters. The flow over a hemisphere was investigated in the low magnetic Reynolds number approximation, with an imposed dipole field. Simulations show that the application of magnetic field slows down the flow in the conductive shock layer and consequently causes the shock wave to move away upstream from the blunt body. The shock standoff distance predicted in the present simulation coincides perfectly with another numerical solution reported in literature. Bush's analysis[3] tends to underpredict the standoff distance, but it becomes more accurate for higher shock density ratios. Inviscid, resistive flow over a circular cylinder has been computed using the full MGD equations. Good agreement with the existing numerical solutions has been obtained. Increase in the shock distance and reduction in the surface pressure with increasing magnetic field have been observed. However, no change in total pressure is noticed, thus suggesting no change in wave drag. The magnetic Reynolds number has a great impact on the flow structure. For a resistive fluid, the flow does not exhibit radically new features. On the other hand, for ideal conducting fluid, secondary waves corresponding to sharp expansions are detected near the body surface, where the magnetic field is confined.

Inclusion of chemistry effects in the simulation of hypersonic flow results in higher density ratio, lower temperature ratio across the shock wave, and reduced shock standoff distance. The effect on the postshock pressure is minimal. At low altitudes, the flow is mostly in chemical equilibrium, although small nonequilibrium regions exist immediately downstream of the shock wave. At higher altitudes, nonequilibrium phenomena dominate the flowfield. At a given altitude, thermal dissociations are enhanced with increasing Mach number. The application of a magnetic field has a significant impact on the chemical kinetics. In particular, the joule heating enhances thermal dissociation of air. This investigation illustrates the importance of high-temperature effects on hypersonic MGD and allows to infer the necessity of implementing accurate thermochemical models for the prediction of heat transfer in a full viscous simulation.

Acknowledgments

This work was sponsored by the Air Force Office of Scientific Research, monitored by John Schmisseur. The authors acknowledge the support of Kansas National Science Foundation Cooperative Agreement EPS-9874732 and the Wichita State University High Performance Computing Center.

References

[1]Resler, E. L., and Sears, W. R., "The Prospects of Magneto-Aerodynamics," *Journal of the Aeronautical Sciences*, Vol. 25, No. 4, 1958, pp. 235–245.

[2]Ziemer, R. W., and Bush, W. B., "Magnetic Field Effects on Bow Shock Stand-Off Distance, Space Technology Laboratory," *Physical Review Letters*, Vol. 1, No. 2, 1958, pp. 58, 59.

[3]Bush, W. B., "Magnetohydrodynamic-Hypersonic Flow Past a Blunt Body," *Journal of the Aero/Space Sciences*, Vol. 25, Nov. 1958, pp. 685–690.

[4]Kemp, N. H., "On Hypersonic Stagnation-Point Flow with a Magnetic Field," *Journal of the Aeronautical Sciences*, Vol. 25, June 1958, pp. 405–407.

[5]Freeman, N. C., "On the Flow Past a Sphere at Hypersonic Speed with a Magnetic Field," *Journal of the Aero/Space Sciences*, Vol. 26, 1959, pp. 670, 671.

[6]Wu, C. S., "Hypersonic Viscous Flow Near the Stagnation Point in the Presence of Magnetic Field," *Journal of the Aero/Space Sciences*, Vol. 27, Dec. 1960, pp. 882–893.

[7]Lykoudis, P. S., "The Newtonian Approximation in Magnetic Hypersonic Stagnation-Point Flow," *Journal of the Aerospace Sciences*, July 1961, pp. 541–546.

[8]Ericson, W. B., and Maciulaitis, A., "Investigation of Magnetohydrodynamic Flight Control," *Journal of Spacecraft and Rockets*, Vol. 1, No. 3, 1964, pp. 283–289.

[9]Romig, M. F., "The Influence of Electric and Magnetic Fields on Heat Transfer to Electrically Conducting Fluids," *Advances in Heat Transfer*, edited by T. F. Irvine Jr. and J. P. Hartnett, Vol. 1, Academic Press, New York, 1964, pp. 267–354.

[10]Kranc, S., Porter, R. W., and Cambel, A. B., "Electrodeless Magnetogasdynamic Power During Entry," *Journal of Spacecraft and Rockets*, Vol. 4, No. 6, 1967, pp. 813–815.

[11]Chen, S. Y., "Magnetic Hypersonic Flow near the Stagnation Point at Low Reynolds Number," *Journal of Spacecraft and Rockets*, Vol. 6, No. 8, 1969, pp. 1062–1067.

[12]Coakley, J. F., and Porter, R. W., "Time-Dependent Numerical Analysis of Magnetohydrodynamics Blunt-Body Problem," *AIAA Journal*, Vol. 9, No. 8, 1971, pp. 1624–1626.

[13]Gurijanov, E. P., and Harsha, P. T., "AJAX: New Directions in Hypersonic Technology," AIAA Paper 96-4609, April 1996.

[14]Bruno, C., and Czysz, P. A., "An Electro–Magnetic–Chemical Hypersonic Propulsion System," AIAA Paper 98-1582, April 1998.

[15]Poggie, J., and Gaitonde, D. V., "Computational Studies of Magnetic Control in Hypersonic Flow," AIAA Paper 2001-0196, Jan. 2001.

[16]Palmer, G., "Magnetic Field Effects on the Computed Flow over a Mars Return Aerobrake," *Journal of Thermophysics and Heat Transfer*, Vol. 7, No. 2, 1993, pp. 294–301.

[17]Augustinus, J., Hoffmann, K. A., and Harada, S., "Effect of Magnetic Field on the Structure of High-Speed Flows," *Journal of Spacecraft and Rockets*, Vol. 35, No. 5, 1998, pp. 639–646.

[18]MacCormack, R. W., "An Upwind Conservation Form Method For the Ideal Magnetohydrodynamics Equations," AIAA Paper 99-3609, June–July 1999.

[19]Gaitonde, D. V., and Poggie, J., "Simulation of MHD Flow Control Techniques," AIAA Paper 2000-2326, June 2000.

[20]Landrum, D., and Candler, G., "Vibration-Dissociation Coupling in Nonequilibrium Flows," AIAA Paper 91-0466, Jan. 1991.

[21]Park, C., "Assessment of Two-Temperature Kinetic Model for Ionized Air," *Journal of Thermophysics and Heat Transfer*, Vol. 3, No. 3, 1989, pp. 233–244.

[22]Tannehill, J. C., and Mugge, P. H., "Improved Curve Fits for the Thermodynamic Properties of Equilibrium Air Suitable for Numerical Computation Using Time-Dependent or Shock Capturing Methods," NASA CR2470, 1974.

[23]Grossman, B., and Cinnella, P., "The Computation of Non-Equilibrium, Chemically-Reacting Flows," *Computers and Structures*, Vol. 30, No. 1/2, 1988, pp. 79–93.

[24]Candler, G. V., and MacCormack, R. W., "The Computation of Hypersonic Ionized Flows in Chemical and Thermal Nonequilibrium," AIAA Paper 88-0511, Jan. 1988.

[25]Gnoffo, P. A., Gupta, R. N., and Shinn, J. L., "Conservation Equations and Physical Models for Hypersonic Air Flows in Thermal and Chemical Nonequilibrium," NASA TP-2867, Feb. 1989.

[26]Damevin, H.-M., and Hoffmann, K. A., "Development of a Modified Runge–Kutta Scheme with Total Variation Diminishing Limiters for Ideal Three-Dimensional Magnetogasdynamics," AIAA Paper 2001-2739, June 2001.

[27]Powell, K. G., "An Approximate Riemann Solver for Magnetohydrodynamics (that Works in More Than One Dimension)," NASA CR 194902, Inst. for Computer Applications in Science and Engineering, ICASE Rept. No. 94-24, April 1994.

[28]Damevin, H.-M., "Development of Numerical Techniques for Simulation of Magnetogasdynamics and Hypersonic Chemistry," Ph.D. Dissertation, Dept. of Aerospace Engineering, Wichita State Univ., Wichita, KS, Dec. 2001.

[29]Porter, R. W., and Cambel, A. B., "Magnetic Coupling in Flight Magnetoaerodynamics," *AIAA Journal*, Vol. 5, No. 4, 1967, pp. 803–805.

[30]Billig, F. S., "Shock-Wave Shapes Around Spherical- and Cylindrical-Nosed Bodies," *Journal of Spacecraft and Rockets*, Vol. 4, No. 6, 1967, pp. 822, 823.

[31]Palmer, H. B., "Chemical Kinetics and Hypersonic Flow," *Fundamental Phenomena in Hypersonic Flow*, edited by G. J. Hall, Cornell Univ. Press, Ithaca, NY, 1966, pp. 175–190.

[32]Wray, K. L., "Prepared Comments," *Fundamental Phenomena in Hypersonic Flow*, edited by G. J. Hall, Cornell Univ. Press, Ithaca, NY, 1966, pp. 190-194.

[33]Gordon, S., and McBride, B. J., "Computer Program for Calculation of Complex Chemical Equilibrium Composition and Applications. Part I-Analysis," NASA RP-1311, 1994.